

Stokes–anti-Stokes correlation in the inelastic scattering of light by matter and generalization of the Bose-Einstein population function

Carlos A. Parra-Murillo, Marcelo F. Santos, Carlos H. Monken, and Ado Jorio*

Departamento de Física, Universidade Federal de Minas Gerais, Belo Horizonte, Minas Gerais 31270-901, Brazil

(Received 24 July 2015; revised manuscript received 17 January 2016; published 28 March 2016)

The Stokes and anti-Stokes components in the inelastic scattering of light are related to phonon statistics and have been broadly used to measure temperature and phonon lifetimes in different materials. However, correlation between the components is expected to change the Stokes/anti-Stokes intensity ratio, imposing corrections to the broadly used Bose-Einstein statistics. In this work the excitation power dependence of these scattering processes is theoretically described by an effective Hamiltonian that includes correlation between the Stokes and the anti-Stokes events. The model is used to fit available experimental results in three-dimensional diamond and two-dimensional graphene, showing that the phenomenon can significantly increase in the low-dimensional system under specific resonance conditions. By setting the scientific basis for the Stokes–anti-Stokes correlated phenomenon, the use of the Bose-Einstein population function to determine the inelastic scattering is generalized, providing a model to predict the conversion of optical phonons into heat or light, according to coupling constants and decay rates. The model applies to inelastic scattering in general.

DOI: [10.1103/PhysRevB.93.125141](https://doi.org/10.1103/PhysRevB.93.125141)

I. INTRODUCTION

The inelastic scattering of light by matter [1] exhibits two components: the *Stokes* (S) event, where an incident photon is converted into a phonon and a redshifted S photon, and the *anti-Stokes* (aS) event, where one incident photon and one existing phonon are annihilated, generating a blueshifted aS photon. The Stokes/anti-Stokes intensity ratio is a signature of the quantum character of lattice vibrations, considered to be defined by the Bose-Einstein distribution

$$\frac{I_{aS}}{I_S} = C \frac{n_0}{1 + n_0}, \quad (1)$$

where C depends on the optical properties of the sample and experimental setup, and $n_0 = (e^{\frac{\hbar\nu}{k_B T}} - 1)^{-1}$ is the effective phonon population [2]. $n_0 \ll 1$ for phonons with energies ($\hbar\nu$) larger than the thermal energy $k_B T$ (k_B is the Boltzmann constant). The I_{aS}/I_S intensity ratio is used to measure phonon lifetimes [3,4], local effective temperatures [5,6], and optical resonances [7], and except for very specific resonance conditions the I_{aS}/I_S ratio should approach unity only if the temperature is high enough to activate a very large phonon population. However, Klyshko [8,9] proposed a correlated process, called here the *Stokes–anti-Stokes* (SaS) event, where a phonon created by the Stokes process is subsequently annihilated in the anti-Stokes process. If the SaS event is significant, the picture described by the Bose-Einstein phonon distribution is not complete, and Eq. (1) has to be generalized. The S , aS , and SaS processes are summarized in the Feynman diagrams of Fig. 1, as introduced by Ref. [10].

Evidence for the SaS process is accumulating in materials science [3,4,6,10–12], generating interests in quantum optics [11,12]. Lee *et al.* [11] demonstrated the quantum nature of the SaS correlation in diamond by measuring a nonclassical SaS field correlation function $g^{(2)}$. Klyshko [9] pointed that

the correlated character of this S and aS photons can be continuously varied from purely quantum to purely classical, and Kasperczyk *et al.* [12] explored this transition in character by changing the photon and phonon reservoirs through changes in the excitation laser power. While these experiments are usually performed with ultrafast pulsed lasers to enhance the response of the nonlinear SaS event, Jorio *et al.* [10] have provided evidence of the observation of a dominant SaS event using a few-milliwatt continuous wave (CW) laser; i.e., results are achievable even with a simple laser pointer. This result was obtained in twisted-bilayer graphene (tBLG), a two-dimensional system specially engineered to exhibit resonance with the aS photon emission [10]. Since phonons have a significant lifetime, it has been proposed that these systems can work as a solid state quantum memory, storing information between the write (Stokes) and read (anti-Stokes) processes [11]. In diamond and graphene, $\hbar\nu \gg k_B T$ and the quantum memory would be able to work at room temperature.

In this work an effective Hamiltonian that includes correlation between the Stokes and the anti-Stokes events is proposed to study the excitation power dependence of these scattering processes (see Sec. II). The model is then used to fit available experimental results in three-dimensional diamond and two-dimensional graphene (see Sec. III). The concluding remarks are presented in Sec. IV.

II. THEORETICAL ANALYSIS

A. The theoretical model

Here the I_{aS}/I_S -based phonon population analysis is generalized by proposing an effective Hamiltonian that explicitly considers the Stokes and anti-Stokes fields' correlation, on a simple formalism that is able to fit the experimental results from diamond and graphene. The Hamiltonian is given by [13]

$$\begin{aligned} \hat{H} = & \hbar\omega_0 \hat{a}^\dagger \hat{a} + \hbar\nu \hat{c}^\dagger \hat{c} + \hbar\omega_S \hat{b}_S^\dagger \hat{b}_S + \hbar\omega_{aS} \hat{b}_{aS}^\dagger \hat{b}_{aS} \\ & + \hbar\lambda_S (\hat{a} \hat{c}^\dagger \hat{b}_S^\dagger + \text{H.c.}) + \hbar\lambda_{aS} (\hat{a} \hat{c} \hat{b}_{aS}^\dagger + \text{H.c.}), \quad (2) \end{aligned}$$

*Correspondence should be addressed to: adojorio@fisica.ufmg.br

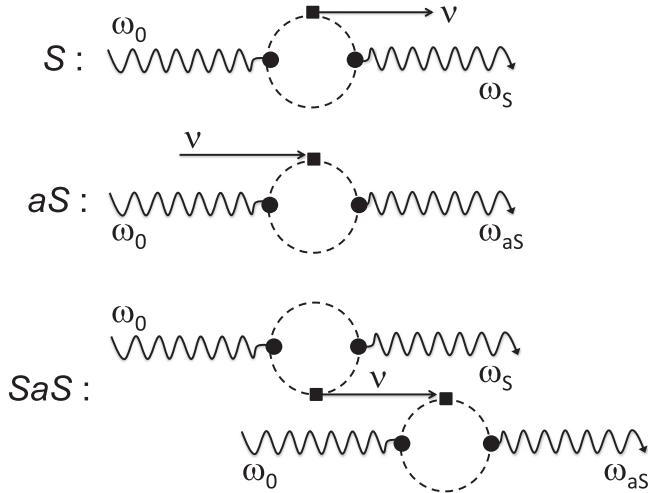


FIG. 1. Feynman diagrams for the Stokes (S), anti-Stokes (aS), and Stokes–anti-Stokes (SaS) Raman scattering processes [10]. Wavy and straight arrows stand for photons and phonons, respectively. Dashed circles represent electron-hole pairs, while black dots and black squares represent electron-photon and electron-phonon interactions, respectively. ω_0 and ν are the incident and the phonon fields frequencies, respectively, and $\omega_{S,aS}$ are the S,aS scattered field frequencies.

where $\hat{b}_{S,aS}$ ($\hat{b}_{S,aS}^\dagger$), \hat{c} (\hat{c}^\dagger), and \hat{a} (\hat{a}^\dagger) represent the annihilation (creation) operator of Stokes (S), anti-Stokes (aS), phonon (c), and incident (a) fields, respectively. λ_S and λ_{aS} are the coupling constants. The λ_S coupling term describes the creation of an S photon and a phonon through the absorption of an incident photon, and the λ_{aS} term describes the creation of an aS photon through the absorption of an incident photon and a phonon. ω_0 and ν are the incident and the phonon fields frequencies, respectively, so the Stokes and anti-Stokes modes have energies given by $\hbar\omega_{aS,S} = \hbar\omega_0 \pm \hbar\nu$. Typically, the coherent sources used in experiments of this type can be considered to have a large enough number of photons, which allows us to replace $(\hat{a}, \hat{a}^\dagger) \rightarrow (\alpha, \alpha^*)$, with $|\alpha|^2$ being the mean number of incident photons. The laser power is given by $P_L = \mathcal{A}|\alpha|^2$, \mathcal{A} being a constant with power units, depending on the laser frequency and temporal mode distribution. The Hamiltonian model above is valid within the coherence time of the pumping laser, whether continuous or pulsed.

Hamiltonian (2) accounts for the interaction at the material but it does not properly describe the dissipation of the created excitations due to the presence of the photonic and phononic reservoirs. Such dynamics can be computed by means of the Markovian master equation [14] for the overall reduced density operator of the three fields, introducing decay rates of phonons and scattered photons. The master equation for the density operator $\hat{\rho} = \text{Tr}_R \hat{\rho}_{\text{total}}$, in the Lindblad form, reads

$$\frac{d}{dt} \hat{\rho} = -i[\hat{H}, \hat{\rho}] + \mathcal{L}(\hat{\rho}), \quad (3)$$

where Tr_R indicates the tracing out of the reservoir degrees of freedom. The Lindbladian term in our model is $\mathcal{L} = \mathcal{L}_b + \mathcal{L}_c$,

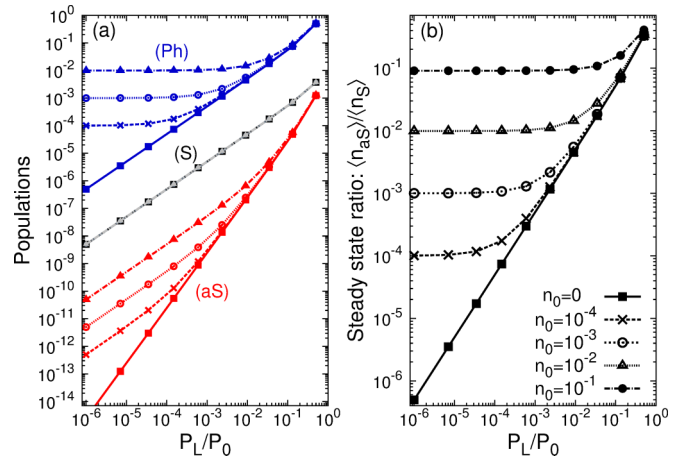


FIG. 2. Panel (a) presents Stokes (S), anti-Stokes (aS), and phonon (Ph) populations as a function of the laser power P_L . We set $\lambda_S = \lambda_{aS} = \lambda$, $\gamma_S = \gamma_{aS} = \gamma$, and P_L is given in units of P_0 , with $P_0 \approx \mathcal{A}\gamma\gamma_c/2\lambda^2$ for $\gamma/\gamma_c \gg n_0$. P_0 in power units. The stationary phonon population gives nonphysical description for $P_L \geq P_0$ (see Appendix A for more details about P_0). The different curves correspond to different temperatures set by the thermal average number n_0 [see legend in panel (b)]. In panel (b) we show the ratio between aS and S mode population as a function of P_L and n_0 . For this figure we set $\tilde{\gamma} = \gamma/\gamma_c = 100$ and a continuous pumping.

with

$$\begin{aligned} \mathcal{L}_b(\hat{\rho}) &= - \sum_{x=S,aS} \gamma_x (\hat{b}_x^\dagger \hat{b}_x \hat{\rho} + \hat{\rho} \hat{b}_x^\dagger \hat{b}_x - 2\hat{b}_x \hat{\rho} \hat{b}_x^\dagger), \\ \mathcal{L}_c(\hat{\rho}) &= -\gamma_c (n_0 + 1) (\hat{c}^\dagger \hat{c} \hat{\rho} + \hat{\rho} \hat{c}^\dagger \hat{c} - 2\hat{c} \hat{\rho} \hat{c}^\dagger) \\ &\quad - \gamma_c n_0 (\hat{c} \hat{c}^\dagger \hat{\rho} + \hat{\rho} \hat{c} \hat{c}^\dagger - 2\hat{c}^\dagger \hat{\rho} \hat{c}), \end{aligned} \quad (4)$$

with γ_S , γ_{aS} , and γ_c being the decay rates (proportional to the inverse of the coherence time) of the respective Stokes, anti-Stokes, and phonon fields. To analyze the Stokes and anti-Stokes field intensities and their respective correlation functions at zero delay ($\tau = 0$), we compute the average values

$$\begin{aligned} \langle n_{S,aS} \rangle &= \langle \hat{b}_{S,aS}^\dagger \hat{b}_{S,aS} \rangle, \quad \langle n_c \rangle = \langle \hat{c}^\dagger \hat{c} \rangle, \\ g^2(0) &= \frac{\langle \hat{b}_S^\dagger \hat{b}_{aS}^\dagger \hat{b}_{aS} \hat{b}_S \rangle}{\langle \hat{b}_S^\dagger \hat{b}_S \rangle \langle \hat{b}_{aS}^\dagger \hat{b}_{aS} \rangle}. \end{aligned} \quad (5)$$

B. Numerical simulations

Here the results from numerical simulations of Eqs. (5) will be discussed. For details about the implementation, see Appendix A.

Setting $\lambda_S = \lambda_{aS} = \lambda$, $\gamma_S = \gamma_{aS} = \gamma$, $\lambda|\alpha|/\gamma_c \neq 0$, and considering the limit of $\gamma/\gamma_c \gg n_0$, Fig. 2 presents how the phononic and photonic populations depend on the laser power P_L for different thermal phonon numbers n_0 . While the Stokes field is found to be proportional to the excitation laser power P_L , the anti-Stokes field exhibits two different regimes. For lower power, thermal phonons dominate the process and $\langle n_{aS} \rangle$ is proportional to P_L (assuming there is no laser induced heating). For higher powers, the SaS phenomenon dominates, and $\langle n_{aS} \rangle$ is proportional to P_L^2 . This rationale explains the

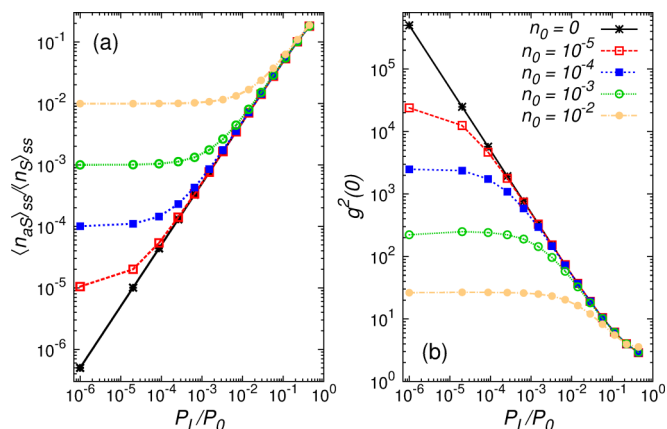


FIG. 3. Theoretical description of the anti-Stokes/Stokes intensity ratio and the correlation phenomena. (a) gives the population ratio $\langle n_{aS} \rangle_{ss} / \langle n_S \rangle_{ss}$, where ss stands for steady state, and (b) gives the SaS field correlation $g^2(0)$, according to Eqs. (5). The excitation laser power P_L dependences are plotted for different values of the thermal phonon population n_0 [see legend in (b)]. As in Fig. 2, we set $\lambda_S = \lambda_{aS} = \lambda$, $\gamma_S = \gamma_{aS} = \gamma$, and $P_0 \approx \mathcal{A}\gamma\gamma_c/2\lambda^2$ for $\gamma/\gamma_c \gg n_0$.

results in Fig. 2(b), I_{aS}/I_S being constant for low power, and for high power $I_{aS}/I_S \propto P_L$.

The two regimes are also reflected in the results for cross-correlation function $g^2(0)$, as shown in Fig. 3. The power dependence for the intensity ratio I_{aS}/I_S and the SaS correlation $g^2(0)$ are described in panels (a) and (b) of Fig. 3, respectively, for different values of the thermal phonon population n_0 . In Fig. 3(b), the SaS correlation function $g^2(0)$ is shown to be proportional to the inverse laser power, and it goes to an n_0 -dependent constant value for small values of P_L .

So far our analysis has been done for continuous pumping, which allows for well-behaved steady state solutions. When considering a time-dependent but short-time pumping, the system response is similar in shape to the implemented pulse and a steady state is not expected. In that case, we computed the long-time averages of the observables of interest (see Appendix A for details on continuous vs short-time pumping implementation). The results for the photonic populations are shown in Fig. 4 in comparison with the steady state solution for continuous pumping. It is clearly seen that the phenomenology studied throughout this paper is preserved; that is, the different regimes of the populations with increasing laser power P_L are preserved, and only changes in the intensity of the S and aS modes are observed. The results in Fig. 4 allow us to generalize the findings presented in this work to experiments with pulsed lasers.

C. Generalization of the I_{aS}/I_S figure of merit

A rationale for I_{aS}/I_S that takes into account the SaS phenomenon can be developed based on the theory for $\langle n_{aS} \rangle_{ss} / \langle n_S \rangle_{ss}$. Here, $\langle n_{S,aS} \rangle_{ss}$ is the steady state number of S , aS photons. In the previous analysis, we set the Stokes, λ_S , and anti-Stokes, λ_{aS} , couplings to be the same for simplicity. However, in general, that is not the case, and from now on we will consider their relation to be given by $\lambda_{aS}^2 = \epsilon \lambda_S^2$, ϵ being a material-dependent parameter to be determined by the

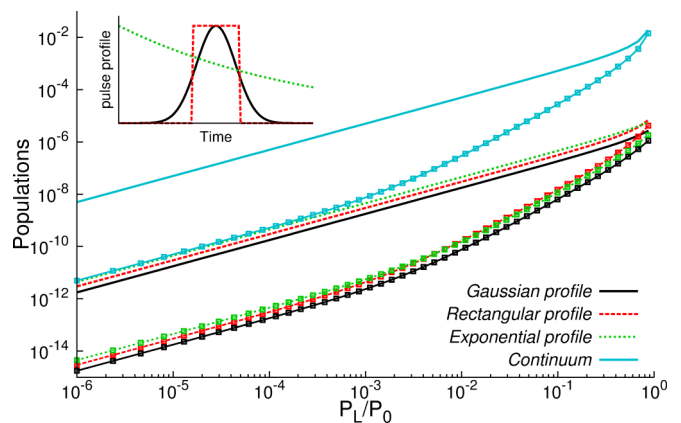


FIG. 4. Stokes (lines) and anti-Stokes (lines with squares) mode populations as a function of the normalized laser power (P_L/P_0) for different types of incident laser (see legend). The inset shows the time profile of the implemented lasers. The parameters are same as those in Fig. 2, with $n_0 = 10^{-3}$.

experimental data. The linewidths of the two fields will still be taken to be equal, i.e., $\gamma_S = \gamma_{aS} = \gamma$ and $r = \gamma/\gamma_c \gg n_0$, a condition matched in the experiments. Finally, the anti-Stokes/Stokes intensity ratio is given by (see Appendix A for details)

$$\frac{\langle n_{aS} \rangle_{ss}}{\langle n_S \rangle_{ss}} = \epsilon \frac{n_0}{n_0 + 1} + C_{SaS} P_L \left[\frac{1}{n_0 + 1} - \epsilon \frac{n_0}{(n_0 + 1)^2} \right] \frac{2r + 1}{2r + 2}, \quad (6)$$

where $C_{SaS} = \frac{|\lambda_{aS}|^2}{\gamma\gamma_c\mathcal{A}}$ gives the effective response of the anti-Stokes line ($\frac{|\lambda_{aS}|^2}{\gamma\gamma_c}$) per unit of pumping power. Notice that $C_{SaS} = 2/P_0$, and although they are simply related, we keep them both here because they have different meanings: C_{SaS} is a ready-to-use fitting parameter, while P_0 gives the limit of validity of our phonon calculations. Both ϵ and C_{SaS} depend on the optical parameters, for instance, absorption coefficients, inelastic scattering cross sections, and the dimensions (geometry) of the sample under study [15]. In Eq. (1), which gives the ratio between the response of the anti-Stokes and Stokes fields driven solely by thermal phonons [limit of zero pump power in Eq. (6)], the constant C is proportional to ϵ , but it can also include the different optical setup responses for the Stokes and anti-Stokes photons. Furthermore, when measuring intensity ratios, a factor $(\omega_{aS}^3/\omega_S^3)$ has to be considered. However, when using photon counting devices, such as a charged coupled device (CCD) or a avalanche photo-diode (APD), the detectors are counting photon-related events and the $(\omega_{aS}^3/\omega_S^3)$ term should not be included.

As a final comment, for completeness, the I_{aS}/I_S dependencies actually have a quadratic term in P_L , which has been neglected in Eq. (6) because the term $\propto P_L^2$ is irrelevant in the range of pumping parameters exploited in the experiments. The full derivation of the I_{aS}/I_S equations can be found in Appendix A, and a quantitative analysis demonstrating the quadratic-term irrelevance can be found in the Appendix B.

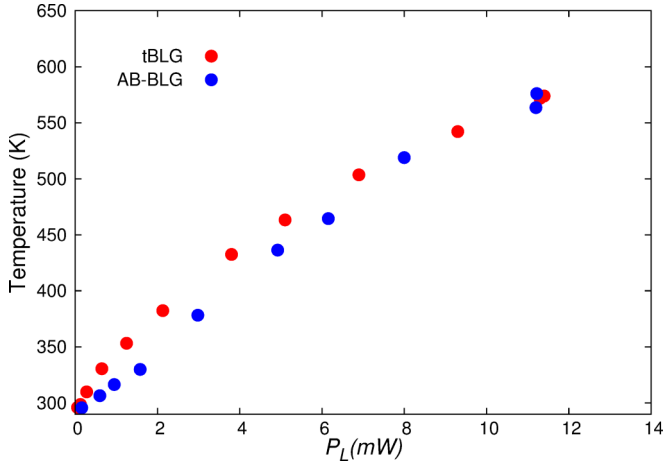


FIG. 5. Expected effective temperature T for tBLG (red) and AB-BLG (blue), extracted directly from the I_{aS}/I_S data in Ref. [10], according to Eq. (7), which neglects the SaS phenomena.

III. ANALYSIS OF EXPERIMENTAL DATA

A. Failure of the Bose-Einstein population analysis

Qualitatively, the behaviors of I_S , I_{aS} and $g^2(0)$ observed by Kasperczyk *et al.* [12] are described by the steady state numbers of S and aS photons, $\langle n_S \rangle_{ss}$ and $\langle n_{aS} \rangle_{ss}$, and by $g^2(0)$, calculated by considering the model in Eqs. (2)–(5). In this case, the I_{aS}/I_S intensity ratio will not necessarily obey the broadly used Eq. (1).

The failure of the Bose-Einstein population in the analysis of I_S and I_{aS} [Eq. (1)] becomes particularly evident in two-dimensional graphene, as discussed in Ref. [10], where the authors compare the results from two types of samples: a bilayer graphene, where the layers are superposed in the so-called AB-stacking configuration (AB-BLG) [10], and a twisted bilayer graphene (tBLG), which was engineered to exhibit electronic resonance with the aS photon emission [10]. Figure 5 is a plot of what would be the effective G -band phonon temperature T for the two graphene samples reported in Ref. [10], if extracted directly from the I_{aS}/I_S experimental data and using the Bose-Einstein phonon distribution function, which from Eq. (1) is given by

$$T = \frac{\hbar\nu}{k_B [\ln C - \ln \frac{I_{aS}}{I_S}]}, \quad (7)$$

where C is chosen such that $T \rightarrow 295$ K as $P_L \rightarrow 0$. For the tBLG data we obtain $C^{\text{tBLG}} = 26$ and for the AB-BLG data we obtain $C^{\text{AB-BLG}} = 4$. The fact that $C^{\text{tBLG}} > C^{\text{AB-BLG}}$ is expected, since tBLG was engineered for specific resonance behavior. However, the fact that T is generally larger for tBLG (red bullets in Fig. 5) compared to AB-BLG (blue bullets in Fig. 5) is not expected. First, the tBLG was engineered for resonance with the anti-Stokes photon emission. Therefore it is expected that this sample would have a stronger cooling channel and that it would actually exhibit lower temperatures than the AB-BLG. Second, a lower phonon frequency redshift is observed for tBLG compared to AB-BLG [10], indicating the heating in tBLG is indeed smaller [16]. Therefore, there is no reason for the tBLG to be hotter than the AB-BLG, and the

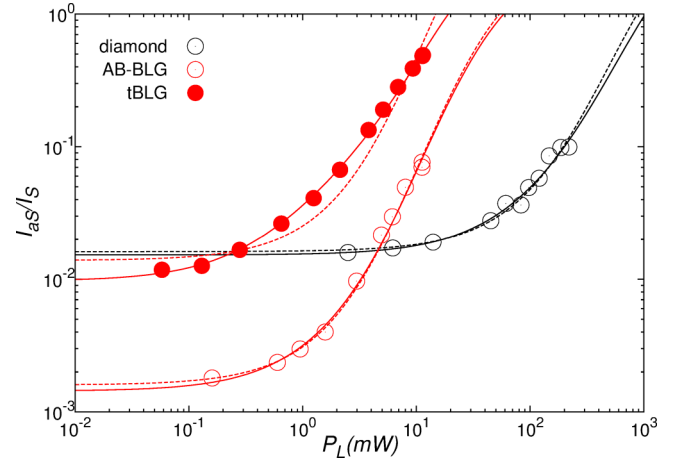


FIG. 6. Fitting the I_{aS}/I_S intensity ratios in three different solid state systems: three-dimensional diamond (open black circles), two-dimensional AB-staked bilayer graphene (AB-BLG, open red circles), and two-dimensional twisted bilayer graphene (tBLG, solid red circles). Data points are experimental results from Ref. [12] (diamond) and Ref. [10] (graphene systems), and the solid lines are fits to the data using Eq. (6) and the parameters listed in Table I. Dashed lines are the fits using just a pump-dependent temperature model, corresponding to Eq. (1).

result obtained with Eq. (7) and displayed in Fig. 5 seems to be inconsistent. Finally, the AB-BLG data can be nicely fit with a simple linear dependence of temperature on the excitation laser power, while the tBLG data require a nonlinear dependence. In the next section we show that all these apparently inconsistent result are harmonized if we consider the SaS event.

B. The I_{aS}/I_S figure of merit

Figure 6 shows a comparison of the experimental I_{aS}/I_S results from the three-dimensional diamond (open black circles) [12], from the AB-staked two-dimensional bilayer graphene (AB-BLG, open red circles) [10] and from the two-dimensional twisted bilayer graphene (tBLG, solid red circles) [10]. The three different results observed for the three different samples in Fig. 6 can all be fit with Eq. (6). The fitting parameters are provided in Table I. The plot also includes the respective fitting curves obtained from the simpler pump-dependent temperature model [Eq. (1)] for the sake of comparison. In Figure 7, we present the separate contribution from the thermal phonons considering laser induced heating [dashed blue lines, first term of Eq. (6)] and from the SaS phenomena without considering laser induced heating [dotted black lines, Eq. (6) with T constant at room temperature] to the I_{aS}/I_S data fitting (solid black lines) for diamond (a), tBLG (b), and AB-BLG (c), using the data from Table I.

Analysis of the data and the fittings shows three separate cases:

(1) In diamond, the I_{aS}/I_S behavior is reasonably influenced by the SaS process, specially for the intermediate pump powers [see Fig. 7(a)], and this is well established in Ref. [12]. However, we must stress that, in this case, I_{aS}/I_S is not a strong figure of merit due to its small variation within the measured range. The nonresonant bulk material takes too long to heat

TABLE I. Parameters used to fit the data from the three materials depicted in Fig. 6, using Eq. (6). C_{SaS} is given in mW^{-1} ($\lambda_S, \lambda_{aS}, \gamma, \text{ and } \gamma_c$ are all in $1/\text{s}$ units) and ϵ is dimensionless. Temperature T , given in K, follows the equation $T = T_0 + bP_L$, with b given in K/mW .

Material	ϵ	$C_{SaS} \equiv (\lambda_{aS}^2/\gamma\gamma_c)A^{-1}$ (mW^{-1})	T (K)
diamond ^a	(5.8 ± 0.5)	$(1.0 \pm 0.9) \times 10^{-4}$	$295 + (0.52 \pm 0.09)P_L$
tBLG	(22 ± 1)	$(3.9 \pm 0.3) \times 10^{-2}$	$295 + (23.2 \pm 0.8)P_L$
AB-BLG	(3.3 ± 0.5)	$(7 \pm 8) \times 10^{-4}$	$295 + (28 \pm 2)P_L$

^aFor the diamond, the measured $\epsilon = (10.1 \pm 0.9)$ was overvalued by a factor of 1.71 due to the difference in efficiency of the CCD detector, 95% vs 60%, and transmittance of the diffractive grating, 83% vs 77%, at the anti-Stokes and Stokes frequencies, respectively (information given by the authors of Ref. [12]). This correction was already taken into account when collecting the data for the graphene experiments [10].

up and the SaS events are rather rare, observable only with femtosecond lasers. These aspects are reflected in the large error for the C_{SaS} value, given in Table I.

(2) For the AB-stacked bilayer graphene (AB-BLG), the I_{aS}/I_S power dependence is dominated by heating, with a linear dependence of the effective phonon temperature on laser power ($T [\text{K}] = 295 + 28P_L [\text{mW}]$), consistent with Fig. 5. The error for the fitted C_{SaS} value is larger than the value itself (negative C_{SaS} is nonphysical), indicating that the effect is negligible. Consequently, the curves obtained with the complete model and the purely thermal effect fit the data equally well, showing that it is the contribution from heating that dominates the response of the material throughout the entire range of pump power. This becomes particularly clear in Fig. 7(c) where we see that the curves using Eq. (6) or just its first term (accounting for the purely thermal effects) are basically the same.

(3) For the tBLG, the SaS process clearly dominates. This is the material that shows the largest values of ϵ and C_{SaS} and whose behavior significantly deviates from the one expected solely due to thermal effects, as seen in both Figs. 6 and 7(b). This is expected considering that the tBLG is geometrically arranged to maximize the anti-Stokes response.

Note that both AB-BLG and tBLG can be fit with a linear dependence of temperature on the excitation laser power (see Table I), and that the temperature raise in the AB-BLG is larger than that of the tBLG, which is consistent with the behavior of the G band frequency changes measured in both materials [10].

As a final consideration, one could still argue whether the unusual I_{aS}/I_S power behavior for tBLG could be explained by a thermal shift of the optical transition energy, which would cause a change in ϵ . Such a shift has been studied for the

one-dimensional van Hove singularities in carbon nanotubes. Within the temperature range that takes place in the tBLG experiment (about 300 K according to the G band shift [10]), redshifts of less than 20 meV were predicted [17] and confirmed experimentally [18]. Such a shift is irrelevant given the much larger resonance width for the optical absorption [10] or for the resonance Raman window of tBLG [19], which are over 0.1 eV.

C. Quantitative analysis of the theoretical parameters: the Stokes and anti-Stokes Raman cross sections

A quantitative analysis will be presented here for tBLG, which is the only case where the C_{SaS} is well defined from the anti-Stokes/Stokes ratio. Our model is based on parameters that can be evaluated from the following experimental conditions:

(1) The phonon decay rate is $1/\gamma_c \approx 10^{-12}$ s, given by the G band phonon lifetime [4,20–22].

(2) The scattered photon decay rate $1/\gamma = 1/\gamma_c$, defined by the phonon lifetime because the excitation photons are generated by a CW laser (HNL150L Red HeNe laser system from Thorlabs), with much longer coherence time. When using the femtosecond pulsed laser (the diamond case), $1/\gamma$ will be dominated by the laser width.

(3) At 295 K, $n_0 = 5 \times 10^{-4}$ for the G band ($\omega_G = 1584 \text{ cm}^{-1}$), and the condition $\gamma/\gamma_c \gg n_0$ is satisfied.

(4) The graphene illuminated area is $A \approx 10^{-12} \text{ m}^2$, and the sample thickness is $L = 3.35 \times 10^{-10} \text{ m}$ [2]. Those values can be used to define $A\delta t = A(L/c)$, where c is the speed of light and $\delta t = (L/c)$ is the time the photon interacts with the graphene in normal incidence.

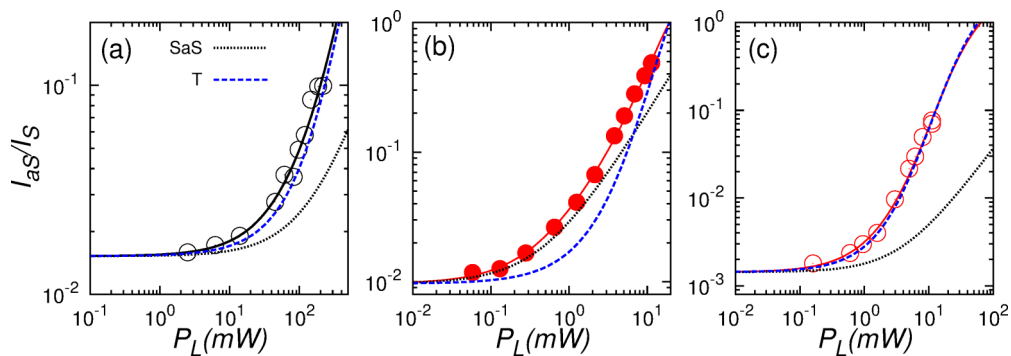


FIG. 7. Contribution from the thermal phonons and from the SaS phenomena in the fitting of I_{aS}/I_S from (a) diamond, (b) tBLG, and (c) AB-BLG. The symbols are the experimental data. The solid lines are the best fits using Eq. (6) from the paper, with the parameters shown in Table I. The dashed blue and the dotted black lines give the separate contributions from the thermal phonons with laser induced heating and from the SaS phenomena without laser induced heating, respectively.

(5) The Raman scattering signal was collected by an objective with numerical aperture $NA = 0.9$, which defines the collection solid angle $\Omega = 3.54$ sr.

(6) The parameter \mathcal{A} relating the mean number of photons $|\alpha|^2$ with the laser power P_L is given by $\mathcal{A} = \hbar\omega_0 N \Delta\nu$, where $\Delta\nu$ is given by the spectral width of one laser frequency mode and N is the number of modes inside the laser coherence time. For the HNL150L Red HeNe laser system, $\Delta\nu \approx 1$ kHz, $N \approx 5$, and $\mathcal{A} \approx 1.57 \times 10^{-12}$ mW.

The value of the anti-Stokes coupling constant λ_{aS} can be calculated using the value obtained for C_{SaS} in Table I and the values provided above, while λ_S can be calculated from λ_{aS} and the value for ϵ in Table I. The Stokes and anti-Stokes cross-sections can also be calculated, considering $\sigma_{aS} = (|\lambda_{aS}|^2/\gamma)A\delta t$ and $\sigma_S = \sigma_{aS}/\epsilon$. Here the differential cross sections for the G band Raman scattering $\sigma_{aS} \approx 10^{-32}$ m² and $\sigma_S \approx 10^{-33}$ m² are found, the latter in excellent agreement with the measured Stokes differential cross section in nanographite [23].

IV. CONCLUDING REMARKS AND GENERALIZATION OF THE BOSE-EINSTEIN POPULATION FUNCTION

Comparing the graphene samples, while in AB-BLG the generated phonons are mostly converted into heat, in tBLG they are mostly converted into light (aS photons). But the most striking result is the much larger efficiency of the SaS process in tBLG, with a $C_{SaS} = (\lambda_{aS}^2/\gamma\gamma_c)\mathcal{A}^{-1}$ value that is two orders of magnitude larger than in bulk diamond. Besides this two orders of magnitude difference, the P_L^2 dependence for I_{aS} in diamond can only be observed with the use of femtosecond lasers [24], where the pulse intensity is about 10^5 times larger than the intensity of continuous wave laser radiation of the same average power. Furthermore, in bulk diamond the number of active atoms in the focal volume is $\sim 10^7$ times larger than in the two-dimensional graphene system. Finally, the ratio I_{aS}/I_S at the highest power in tBLG reaches values of ~ 0.5 , while in diamond $I_{aS}/I_S \sim 0.1$ was reached. Putting all numbers together indicates that correlated SaS generation per involved atom in the graphene-based system is much more efficient than in bulk diamond.

Qualitatively, the reason for the striking efficiency of correlated SaS Raman scattering in the twisted bilayer graphene system might be related to a reduction in phase space in the scattering event. In real space, the confined two-dimensional structure, which enhances electron-hole interactions in low-dimensional structures [25,26], leads to a large overlap between the photon and phonon wave functions. In reciprocal space, the logarithmically diverging two-dimensional Van Hove singularity at the hexagonal saddle (M) point [27] strongly enhances the generation and recombination of electron-hole pairs at the aS photon energy [10,28]. The SaS event is also expected to play a role in other low-dimensional materials [29], where phase-space reduction becomes important.

Raman spectroscopy is established as an important tool to study and characterize nanostructures [2]. By setting the scientific basis for the SaS phenomenon, the use of the Bose-Einstein population function for determining the inelastic scattering is generalized, providing a model to predict the

conversion of optical phonons into heat or light, according to coupling constants and decay rates. It is surprising that the correlation between the Stokes and the anti-Stokes components can seriously affect I_{aS}/I_S , being measurable indirectly from the intensity ratio. This aspect made it possible to measure the importance of the SaS correlation in graphene, where a direct $g^2(0)$ measurement is not possible due to ultrafast luminescence [30,31].

The stationary phonon population can then be analytically obtained from the steady state solution of Eq. (3) and, in the limit of $\gamma/\gamma_c \gg n_0$, it is given by (see Appendix A for details)

$$\begin{aligned} \langle n_c \rangle_{ss} \approx n_0 + \frac{r}{r+1} [1 - n_0(\epsilon - 1)] \frac{C_{SaS}}{\epsilon} P_L \\ - [r + n_0(\epsilon - 1)] \left(\frac{\epsilon - 1}{r + 1} \right) \frac{C_{SaS}^2}{\epsilon^2} P_L^2. \end{aligned} \quad (8)$$

The phonon population has three contributions: the first one is purely thermal and the other two are related to the SaS phenomenon, each contribution dominating at different excitation power ranges (see a plot of $\langle n_c \rangle_{ss}$, indicated as Ph in Fig. 2). Note that the contribution proportional to the pump power can either *heat up* or *cool down* the phonon population, depending on how large ϵ is when compared to n_0 . Heating comes from Stokes processes and cooling from anti-Stokes, and both include spontaneous and stimulated contributions. On the other hand, the second-order term in P_L is always cooling down the population as long as the anti-Stokes process is stronger than the Stokes one, $\epsilon > 1$. This equation is only valid for low pump powers, as we know from the full solution that, for very large power, $\langle n_c \rangle_{ss}$ goes to a constant value (for more details, see Appendix A).

Finally, note that the coupling constants and the decay rates governing the phenomena can themselves be dependent on temperature, through anharmonicities or electron-phonon scattering. On the other hand, the SaS event is an important decay channel that has to be explicitly considered when using Raman spectroscopy to extract structural and transport properties related to phonon scattering in low-dimensional structures [32–34].

More generally, since the Stokes and anti-Stokes components are common to inelastic scattering processes in general, the model is not limited to the Raman scattering by phonons. It is generic, for instance applying also to the scattering of He Atoms on surfaces, to the inelastic neutron scattering, etc. Experimental and theoretical work is needed to address the physics of the $\lambda_{S,aS}$, $\gamma_{S,aS}$, and γ_c parameters when applied to different materials and scattering phenomena.

ACKNOWLEDGMENTS

A.J. acknowledges Lukas Novotny, Mark Kasperczyk, Achim Hartschuh, Stephanie Reich, and Niclas S. Mueller for helpful discussions. This work had financial support from CNPq (grants 460045/2014-8, 407167/2013-7, 303471/2012-3, 301130/2014-0, and 307481/2013-1).

APPENDIX A: MORE DETAILS ABOUT THE THEORETICAL MODEL

To analyze the Stokes and anti-Stokes populations and their respective correlation functions at zero time delay ($\tau = 0$), we computed the average values in Eq. (5), which can be obtained by means of the equation

$$\frac{\partial}{\partial t} \langle \hat{O} \rangle = i \langle [\hat{H}, \hat{O}] \rangle + \text{Tr}(\hat{O} \mathcal{L} \hat{\rho}), \quad (\text{A1})$$

yielding the following linear system of differential equations:

$$\begin{aligned} \partial_t \langle n_S \rangle &= -2\lambda_S \alpha \text{Im}\{\langle \hat{c} \hat{b}_S \rangle\} - 2\gamma_S \langle n_S \rangle, \\ \partial_t \langle n_{aS} \rangle &= -2\lambda_{aS} \alpha \text{Im}\{\langle \hat{c}^\dagger \hat{b}_{aS} \rangle\} - 2\gamma_{aS} \langle n_{aS} \rangle, \\ \partial_t \langle n_c \rangle &= -2\alpha(\lambda_S \text{Im}\{\langle \hat{c} \hat{b}_S \rangle\} - \lambda_{aS} \text{Im}\{\langle \hat{c}^\dagger \hat{b}_{aS} \rangle\}) \\ &\quad - 2\gamma_c (\langle n_c \rangle - n_0), \\ \partial_t \langle \hat{c} \hat{b}_S \rangle &= -i\alpha[\lambda_S (\langle n_S \rangle + \langle n_c \rangle) + \lambda_{aS} \langle \hat{b}_S \hat{b}_{aS} \rangle] \\ &\quad - (\gamma_c + \gamma_S + i\omega_0) \langle \hat{c} \hat{b}_S \rangle - i\lambda_S \alpha, \\ \partial_t \langle \hat{c}^\dagger \hat{b}_{aS} \rangle &= -i\alpha[\lambda_S \langle \hat{b}_S \hat{b}_{aS} \rangle - \lambda_{aS} (\langle n_c \rangle + \langle n_{aS} \rangle)] \\ &\quad - (\gamma_c + \gamma_{aS} + i\omega_0) \langle \hat{c}^\dagger \hat{b}_{aS} \rangle, \\ \partial_t \langle \hat{b}_S \hat{b}_{aS} \rangle &= -i\alpha(\lambda_{aS} \langle \hat{c}^\dagger \hat{b}_{aS} \rangle + \lambda_S \langle \hat{c} \hat{b}_S \rangle) \\ &\quad - (\gamma_S + \gamma_{aS} + i2\omega_0) \langle \hat{b}_S \hat{b}_{aS} \rangle, \end{aligned} \quad (\text{A2})$$

where we considered the pump to be very large, $\langle a^\dagger a \rangle \gg 1$, and replaced a and a^\dagger by α (taking α to be real with no loss of generality). From now on, we will also consider $\gamma_S = \gamma_{aS} = \gamma$, which corresponds to the experimental conditions.

The dynamics will depend on how the incident field is implemented. In the case of a pulsed laser, it is enough to define the pump amplitude as a time-dependent function $f(t)$. This function can, for instance, be modeled as a temporal Gaussian profile, such as $f(t) = \exp(-t^2/2\sigma^2)$, where the coherence time is proportional to σ . In that case there is no steady state and, in order to analyze the behavior of the field population as a function of the laser power P_L , we might consider measurements at the excitation time, that is, the time at which the population gets its first maximum, or the time-averaged values of the observables defined in Eq. (2) as $\langle \hat{O} \rangle_t = \lim_{\Delta t \rightarrow \infty} \int_0^{\Delta t} \langle \hat{O} \rangle_t dt / \Delta t$.

We first focus on the case of continuous pumping, i.e., constant α , on the material. In this case, the system of differential equations (A2) has a steady state solution due to the environment-induced relaxation. To find it, we write the system in Eq. (A2) as a vectorial differential equation $\partial_t \vec{x} = M \vec{x} + \vec{b}$, where M is a time-independent square matrix and

$$\vec{x}^T = (\langle \hat{n}_S \rangle, \langle \hat{n}_{aS} \rangle, \langle \hat{n}_c \rangle, \langle \hat{c} \hat{b}_S \rangle, \langle \hat{c}^\dagger \hat{b}_{aS} \rangle, \langle \hat{b}_S \hat{b}_{aS} \rangle, \langle \hat{b}_S \hat{b}_{aS}^\dagger \rangle), \quad (\text{A3})$$

$$\vec{b}^T = (0, 0, 2\gamma_c n_0, -i\lambda_S \alpha, i\lambda_S \alpha, 0, 0, 0, 0), \quad (\text{A4})$$

and set $d_t \vec{x}_{ss} = 0$, where ss stands for steady state. To solve this, we invert the matrix M , which is only possible if M is not singular, i.e. if its determinant $\text{Det}(M)$ is different from zero. The solutions are given by $\vec{x}_{ss} = -M^{-1} \vec{b}$. By simple

inspection, it is straightforwardly noticed that the Stokes, anti-Stokes and phonon populations satisfy an equilibrium condition

$$\langle \hat{n}_c \rangle_{ss} - n_0 = \frac{\gamma}{\gamma_c} (\langle \hat{n}_S \rangle_{ss} - \langle \hat{n}_{aS} \rangle_{ss}). \quad (\text{A5})$$

This equation shows that if Stokes and anti-Stokes are produced at the same rate, the only phonons left are the thermal ones. On the other hand, since in general Stokes production is favored over anti-Stokes (as will become clear shortly), whenever these scattering processes take place, the distribution of phonons in the sample is not determined solely by temperature anymore. One of the central results in the paper is to show the behavior of the Stokes–anti-Stokes field intensities in terms of the power of the pumping laser. In the steady state regime, we can obtain an analytical expression for those intensities, $I_{S,aS}$, which are proportional to the average population of the photon modes $\langle \hat{n}_{S,aS} \rangle_{ss}$. For S and aS modes we find

$$\langle n_S \rangle_{ss} = \frac{C_{SaS} P_L}{\epsilon(r+1)} \left[\frac{n_0 + 1 + \frac{C_{SaS} P_L (2r+1)}{2(r+1) + (\epsilon-1) \frac{C_{SaS}}{\epsilon} P_L}}{1 + (\epsilon-1) \frac{C_{SaS}}{\epsilon} P_L} \right], \quad (\text{A6})$$

$$\langle n_{aS} \rangle_{ss} = \frac{C_{SaS} P_L}{r+1} \left[\frac{n_0 + \frac{C_{SaS} P_L (2r+1)}{2(r+1) + (\epsilon-1) \frac{C_{SaS}}{\epsilon} P_L}}{1 + (\epsilon-1) \frac{C_{SaS}}{\epsilon} P_L} \right], \quad (\text{A7})$$

where $r = \frac{\gamma}{\gamma_c}$, $C_{SaS} = \frac{|\lambda|^2}{\gamma \gamma_c \mathcal{A}}$, and $P_L = \mathcal{A} |\alpha|^2$. Note that for low laser power both $\langle n_{S,aS} \rangle_{ss}$ increase linearly with P_L and their ratio will depend basically on that of the spontaneous processes. In order to easily identify different regimes for P_L , the intensity ratio I_{aS}/I_S is a good figure of merit. From the equations above, we derive

$$I_{aS}/I_S \propto \epsilon \frac{n_0 + \frac{C_{SaS} P_L (2r+1)}{2(r+1) + (\epsilon-1) \frac{C_{SaS}}{\epsilon} P_L}}{n_0 + 1 + \frac{C_{SaS} P_L (2r+1)}{2(r+1) + (\epsilon-1) \frac{C_{SaS}}{\epsilon} P_L}}, \quad (\text{A8})$$

which, up to moderate pump $C_{SaS} P_L \ll 1$, reduces to Eq. (6) used in the analysis.

The phonon population can also be analytically obtained from the stationary analysis, and it is given by

$$\langle n_c \rangle = \frac{r \frac{C_{SaS}}{\epsilon} P_L + N_0 (r+1 + (\epsilon-1) \frac{C_{SaS}}{\epsilon} P_L)}{(r+1) [1 + (\epsilon-1) \frac{C_{SaS}}{\epsilon} P_L]}. \quad (\text{A9})$$

Note that if $P_L \neq 0$, which activates the SaS modes, the phonon population is always larger than n_0 , therefore the difference $\langle \hat{n}_S \rangle_{ss} - \langle \hat{n}_{aS} \rangle_{ss} > 0$.

There are additional effects that can sophisticate our effective description. For example, we can also consider effects of phase noise caused by elastic scattering of generated phonons with different momenta. This is done by adding an extra Lindblad term

$$\mathcal{L}'_c(\hat{\rho}) = -\gamma'_c (\hat{n}_c^2 \hat{\rho} + \hat{\rho} \hat{n}_c^2 - 2\hat{n}_c \hat{\rho} \hat{n}_c). \quad (\text{A10})$$

It is easily proven, using Eq. (3), that phase noise does not modify the equations for the populations in Eqs. (A6) and (A7), therefore, the equilibrium condition is preserved. Its main

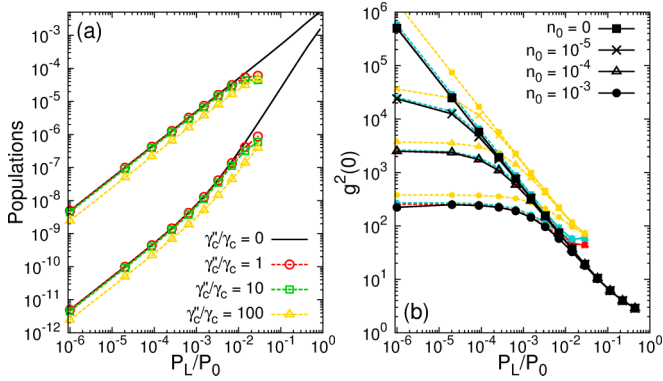


FIG. 8. (a) Stokes (upper lines) and anti-Stokes (lower lines) modes populations as a function of the normalized laser power (P_L/P_0) for different values of γ'_c/γ_c (different line colors, see legend). (b) The effect of γ'_c/γ_c on $g^2(0)$ for different values of n_0 (see legends). Other parameters are same as those in Fig. 2.

changes are for equations of the expected values of the types $\langle \hat{c}^\dagger \hat{b}_{aS} \rangle$ and $\langle \hat{c}^\dagger \hat{b}_{aS} \rangle$, introducing expectation values of second-order operators, for instance $\langle \hat{b}_S \hat{b}_{aS} \rangle$. The new system of equations is not trivial and analytical solutions are no longer easy to obtain. In that case, and for the computation of correlation functions $\langle \hat{b}_x^\dagger \hat{b}_x^\dagger \hat{b}_x \hat{b}_x \rangle$ ($x = S, aS$), we compute the stationary solution for the density operator $\hat{\rho}_{ss}$, for which $d_t \hat{\rho}_{ss} = 0$. We must thus solve $\mathcal{L}_{\text{total}} \hat{\rho}_{ss} = 0$, which requires an expansion in the Fock basis $\{|n_S, n_{aS}, n_c\rangle\} \in \mathcal{H} = \mathcal{H}^S \otimes \mathcal{H}^{aS} \otimes \mathcal{H}^c$. This basis increases exponentially and must be truncated for practical implementations. This is justifiable by the fact that, since P_L/P_0 is always much smaller than 1, the steady state photonic population is never large. After numerically obtaining $\hat{\rho}_{ss}$ we can compute expected values as $\langle \hat{O} \rangle_{ss} = \text{Tr}(\hat{O} \hat{\rho}_{ss})$, and we are able to analyze changes on the population of the photonic modes and SaS correlation functions in terms of the system parameters.

Figure 8 shows that the presence of phase noise ($\gamma'_c \neq 0$) does not affect relevantly the phenomenology presented in this work. Nevertheless, for very large values of P_L the convergence of our numerical fails due to the truncation of the Hilbert space, and the results are not conclusive due to the lack of sufficient resources for tackling that regime.

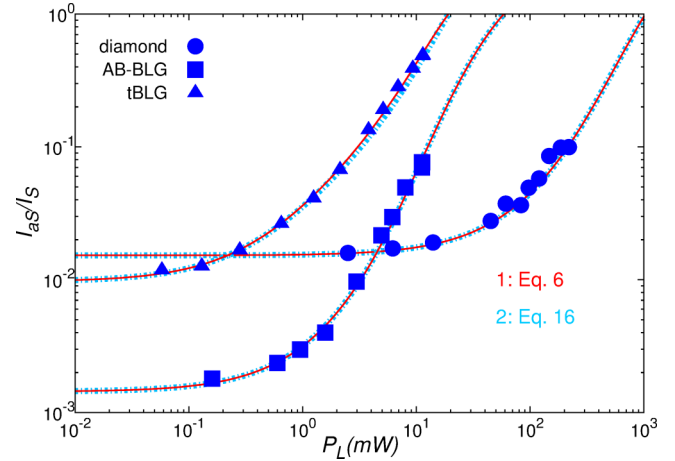


FIG. 9. Fitting of the experimental measurements for the three samples investigated in the paper (symbols - see legend). The red lines come from Eq. (6), plotted using the fitting parameter of Table I. The Dashed light-blue lines correspond to the full equation Eq. (A8).

APPENDIX B: MORE DETAILS ABOUT DATA FITTING

In Fig. 9 we show that the linear fit using Eq. (6) is identical to the full Eq. (A8), before the expansion and approximation, both using the same fitting parameters of Table I. This proves that the quadratic term in the expansion of Eq. (A8) does not introduce any considerable corrections in the power range of experimental interest. In fact, all the experiments are done in the limit $C_{SaS} P_L \ll 1$, so it is reasonable that the linear term in this parameter dominates.

We finally want to remark that our theory is based on phenomenological constants that will depend on the material under study. The validity of the approximations made to obtain analytical expressions for the ratio I_{as}/I_s and the phonon population $\langle n_c \rangle$ is supported by typical and relevant parameters such as n_0 , γ , and γ_c . In typical experiments, like the one reported in Ref. [12], $n_0 = 1.6 \times 10^{-3}$ at $T = 295$ K, $1/\gamma_c \approx 10^{-12}$ s (phonon lifetime) [4,20–22], and $1/\gamma \approx 130 \times 10^{-15}$ s (laser pulse width). The γ/γ_c is at least one order of magnitude larger than 1, and four orders of magnitude larger than n_0 . The incident field has a power range from 1 mW to 1 W and wavelength 785 nm. The number of incident photons is of the order of $|\alpha|^2 \sim 52 \times 10^6 - 52 \times 10^9$ per pulse.

- [1] C. V. Raman and K. S. Krishnan, A new type of secondary radiation, *Nature (London)* **121**, 501 (1928).
- [2] A. Jorio, M. S. Dresselhaus, and R. Saito, *Raman Spectroscopy in Graphene Related Systems* (Wiley-VCH, Weinheim, 2011).
- [3] D. Song, F. Wang, G. Dukovic, M. Zheng, E. D. Semke, L. E. Brus, and T. F. Heinz, Direct Measurement of the Lifetime of Optical Phonons in Single-Walled Carbon Nanotubes, *Phys. Rev. Lett.* **100**, 225503 (2008).
- [4] K. Kang, D. Abdula, D. G. Cahill, and M. Shim, Lifetimes of optical phonons in graphene and graphite by time-resolved incoherent anti-Stokes Raman scattering, *Phys. Rev. B* **81**, 165405 (2010).

- [5] C. Faugeras *et al.*, Thermal conductivity of graphene in Corbino membrane geometry, *ACS Nano* **4**, 1889 (2010).
- [6] S. Berciaud, M. Y. Han, K. F. Mak, L. E. Brus, P. Kim, and T. F. Heinz, Electron and Optical Phonon Temperatures in Electrically Biased Graphene, *Phys. Rev. Lett.* **104**, 227401 (2010).
- [7] A. G. Souza Filho, A. Jorio, J. H. Hafner, C. M. Lieber, R. Saito, M. A. Pimenta, G. Dresselhaus, and M. S. Dresselhaus, Electronic transition energy E_{ii} for an isolated (n, m) single-wall carbon nanotube obtained by anti-Stokes/Stokes resonant Raman intensity ratio, *Phys. Rev. B* **63**, 241404(R) (2001).

- [8] D. N. Klyshko, Correlation between the Stokes and anti-Stokes components in inelastic scattering of light, *Sov. J. Quant. Electron.* **7**, 755 (1977).
- [9] D. N. Klyshko, *Photons and Nonlinear Optics* (Gordon and Breach, New York, 1988).
- [10] A. Jorio *et al.*, Optical-phonon resonances with saddle-point excitons in twisted-bilayer graphene, *Nano Lett.* **14**, 5687 (2014).
- [11] K. C. Lee *et al.*, Macroscopic non-classical states and terahertz quantum processing in room-temperature diamond, *Nat. Photon.* **6**, 41 (2012).
- [12] M. Kasparczyk, A. Jorio, E. Neu, P. Maletinsky, and L. Novotny, Stokes–anti-Stokes correlations in Raman scattering from diamond membranes, *Opt. Lett.* **40**, 2393 (2015).
- [13] T. von Foerster and R. J. Glauber, Quantum theory of light propagation in amplifying media, *Phys. Rev. A* **3**, 1484 (1971).
- [14] H. Carmichael, *An Open Systems Approach to Quantum Optics* (Springer-Verlag, Berlin, 1993).
- [15] H. W. Lo and A. Compeen, Raman Measurement of Lattice Temperature during Pulsed Laser Heating of Silicon, *Phys. Rev. Lett.* **44**, 1604 (1980).
- [16] I. Calizo, A. A. Balandin, W. Bao, F. Miao, and C. N. Lau, Temperature dependence of the Raman spectra of graphene and graphene multilayers, *Nano Lett.* **7**, 2645 (2007).
- [17] R. B. Capaz, C. D. Spataru, P. Tangney, M. L. Cohen, and S. G. Louie, Temperature Dependence of the Band Gap of Semiconducting Carbon Nanotubes, *Phys. Rev. Lett.* **94**, 036801 (2005).
- [18] S. B. Cronin, Y. Yin, A. Walsh, R. B. Capaz, A. Stolyarov, P. Tangney, M. L. Cohen, S. G. Louie, A. K. Swan, M. S. Ünlü, B. B. Goldberg, and M. Tinkham, Temperature Dependence of the Optical Transition Energies of Carbon Nanotubes: The Role of Electron-Phonon Coupling and Thermal Expansion, *Phys. Rev. Lett.* **96**, 127403 (2006).
- [19] V. Carozo, C. M. Almeida, B. Fragneaud, P. M. Bedê, M. V. O. Moutinho, J. Ribeiro-Soares, N. F. Andrade, A. G. Souza Filho, M. J. S. Matos, B. Wang, M. Terrones, R. B. Capaz, A. Jorio, C. A. Achete, and L. G. Cançado, Resonance effects on the Raman spectra of graphene superlattices, *Phys. Rev. B* **88**, 085401 (2013).
- [20] K. Kang, T. Ozel, D. G. Cahill, and M. Shim, Optical phonon lifetimes in single-walled carbon nanotubes by time-resolved Raman scattering, *Nano Lett.* **8**, 4642 (2008).
- [21] H. Yan, D. Song, K. F. Mak, I. Chatzakis, J. Maultzsch, and T. F. Heinz, Time-resolved Raman spectroscopy of optical phonons in graphite: Phonon anharmonic coupling and anomalous stiffening, *Phys. Rev. B* **80**, 121403(R) (2009).
- [22] K. C. Lee, Benjamin J. Sussman, J. Nunn, V. O. Lorenz, K. Reim, D. Jaksch, I. A. Walmsley, P. Spizzirri, and S. Praver, Comparing phonon dephasing lifetimes in diamond using transient coherent ultrafast phonon spectroscopy, *Diam. Relat. Mater.* **19**, 1289 (2010).
- [23] L. G. Cançado, A. Jorio, and M. A. Pimenta, Measuring the absolute Raman cross section of nanographites as a function of laser energy and crystallite size, *Phys. Rev. B* **76**, 064304 (2007).
- [24] A. Jorio *et al.*, Stokes and anti-Stokes Raman spectra of the high energy C-C stretching modes in graphene and diamond, *Phys. Status Solidi B* **252** (11), 2380 (2015).
- [25] K. F. Mak, J. Shan, and T. F. Heinz, Seeing Many-Body Effects in Single- and Few-Layer Graphene: Observation of Two-Dimensional Saddle-Point Excitons, *Phys. Rev. Lett.* **106**, 046401 (2011).
- [26] C. D. Spataru, S. Ismail-Beigi, L. X. Benedict, and S. G. Louie, Excitonic Effects and Optical Spectra of Single-Walled Carbon Nanotubes, *Phys. Rev. Lett.* **92**, 077402 (2004).
- [27] L. Van-Hove, The occurrence of singularities in the elastic frequency distribution of a crystal, *Phys. Rev.* **89**, 1189 (1953).
- [28] A. Jorio and L. G. Cançado, Raman spectroscopy of twisted bilayer graphene, *Solid State Commun.* **175-176**, 3 (2013).
- [29] M. Steiner, H. Qian, A. Hartschuh, and A. J. Meixner, Controlling nonequilibrium phonon populations in single-walled carbon nanotubes, *Nano Lett.* **7**, 2239 (2007).
- [30] C. H. Lui, K. F. Mak, J. Shan, and T. F. Heinz, Ultrafast Photoluminescence from Graphene, *Phys. Rev. Lett.* **105**, 127404 (2010).
- [31] T. Li, L. Luo, M. Hupalo, J. Zhang, M. C. Tringides, J. Schmalian, and J. Wang, Femtosecond Population Inversion and Stimulated Emission of Dense Dirac Fermions in Graphene, *Phys. Rev. Lett.* **108**, 167401 (2012).
- [32] N. Bonini, M. Lazzeri, N. Marzari, and F. Mauri, Phonon Anharmonicities in Graphite and Graphene, *Phys. Rev. Lett.* **99**, 176802 (2007).
- [33] M. Steiner *et al.*, Phonon populations and electrical power dissipation in carbon nanotube transistors, *Nat. Nanotechnol.* **4**, 320 (2009).
- [34] A. Barreiro, M. Lazzeri, J. Moser, F. Mauri, and A. Bachtold, Transport Properties of Graphene in the High-Current Limit, *Phys. Rev. Lett.* **103**, 076601 (2009).